PNAS RESEARCH ARTICLE | CELL BIOLOGY OPEN ACCESS

Epidermal growth factor receptor (EGFR) is a target of the tumor-suppressor E3 ligase FBXW7

Matteo Boretto[a,1], Maarten H. Geurts[a,1], Shashank Gandhi[a,b,1], Ziliang Ma[c,d,e], Nadzeya Staliarova[e], Martina Celotti[a], Sangho Lim[a], Gui-Wei He[a], Rosemary Millen[a], Else Driehuis[a], Harry Begthel[a], Lidwien Smabers[f], Jeanine Roodhart[f], Johan van Es[a], Wei Wu[c,d,e], and Hans Clevers[a,2,3]

Contributed by Hans Clevers; received June 12, 2023; accepted January 8, 2024; reviewed by Rene Bernards and Linda Smit

FBXW7 is an E3 ubiquitin ligase that targets proteins for proteasome-mediated degradation and is mutated in various cancer types. Here, we use CRISPR base editors to introduce different *FBXW7* hotspot mutations in human colon organoids. Functionally, *FBXW7* mutation reduces EGF dependency of organoid growth by ~10,000-fold. Combined transcriptomic and proteomic analyses revealed increased EGFR protein stability in *FBXW7* mutants. Two distinct phosphodegron motifs reside in the cytoplasmic tail of EGFR. Mutations in these phosphodegron motifs occur in human cancer. CRISPR-mediated disruption of the phosphodegron motif at T693 reduced EGFR degradation and EGF growth factor dependency. *FBXW7* mutant organoids showed reduced sensitivity to EGFR-MAPK inhibitors. These observations were further strengthened in CRC-derived organoid lines and validated in a cohort of patients treated with panitumumab. Our data imply that FBXW7 mutations reduce EGF dependency by disabling EGFR turnover.

FBXW7 | organoids | colorectal cancer | EGFR

Significance

Here, we uncover EGFR as substrate of the E3 ubiquitin ligase FBXW7 and found multiple phosphodegron-like motifs within its intracellular domain that when mutated reduce EGFR degradation. FBXW7 mutations contribute to tumorigenesis by reducing EGF dependency. Finally, FBXW7 mutant metastatic colorectal cancer patients showed faster disease progression when treated with anti-EGFR-targeted therapies, suggesting it to be a negative modulator of anti-EGFR therapy response in colorectal cancer.

The ubiquitin–proteasome system (UPS) mediates protein degradation in eukaryotic cells. The sequential activity of a ubiquitin-activating enzyme (E1), ubiquitin-conjugating enzyme (E2), and ubiquitin ligase enzyme (E3) results in the assembly of ubiquitin chains on the substrate proteins and their targeted degradation by the UPS (1, 2). Aberrant activity of the UPS underlies several diseases, including cancer (3–8).

Among the more than 600 E3 ligases encoded in the human genome (9), F-box and WD repeat domain-containing 7 (*FBXW7*) has emerged as a commonly mutated gene across several cancer types (5). FBXW7, also known as hCDC4, is the substrate recognition component of the RING domain-containing SCF-type (SKIP1, CUL1, and F-box protein) ubiquitin ligase (10, 11). It contains three functional domains, i.e., a scaffold SKIP1-binding domain, a dimerization domain, and a substrate binding domain, with the latter being a mutational hotspot in cancer (11, 12). FBXW7 binds to phosphorylated substrates within an evolutionary conserved motif known as Cdc4 phosphodegron (CPD), composed of a central phosphorylated threonine (Thr) or serine (Ser) followed by a second phosphorylation site four amino acids downstream (10, 13–15). The strength of the interaction between FBXW7 and its substrates is not only determined by the optimal CPD sequence (8, 9, 13, 14) but also by the presence of multiple CPDs within the target protein, directing the binding of FBXW7 dimers (12, 13, 15). Yet, the importance of dimerization and the dependence on multiple CPDs remains controversial (10). Previously identified FBXW7 targets include known oncogenes and tumor suppressor genes (14, 16–31). Only a handful of these have been confirmed across studies, likely because of differences between experimental models: immortalized cell lines and models with substantial biological divergence (yeast and mouse).

FBXW7 ranks among the top mutated genes in colorectal cancer (CRC) (32), a leading cause of morbidity and mortality worldwide (33). Despite extensive research, our understanding of the range of FBXW7 substrates and the consequences of its mutations in CRC is incomplete. Recent clinical studies have suggested a correlation between *FBXW7* mutations and poorer clinical outcome (34–36). Wild-type human colon organoids (hCOs) provide a robust model system to study the impact of cancer-associated mutations in a human-relevant settings (37, 38). When combined with genome editing techniques, organoids provide a valuable tool to dissect the biological impact of individual mutations (38, 39). Here, we use CRISPR-Cas9 base editors (40) to introduce *FBXW7* hotspot mutations in human colon organoids to study their functional consequences.

Results

Establishment of an Organoid Biobank of Recurrent *FBXW7* Mutations. *FBXW7* is recurrently mutated across cancer types, yet its mutations are most frequent in CRC (32) when ranked per adjusted mutational rate (Fig. 1*A*). Most hotspot mutations involve simple

Author contributions: M.B., M.H.G., and H.C. designed research; M.B., M.H.G., S.G., Z.M., N.S., M.C., S.L., G.-W.H., R.M., L.S., J.R., and W.W. performed research; E.D., H.B., and J.v.E. contributed new reagents/analytic tools; M.B., M.H.G., S.G., Z.M., N.S., S.L., G.-W.H., L.S., J.R., W.W., and H.C. analyzed data; and M.B. and H.C. wrote the paper.

Reviewers: R.B., Antoni van Leeuwenhoek; and L.S., Amsterdam University Medical Center (UMC) location Vrije University Medical Center (VUmc), Cancer Center Amsterdam.

Competing interest statement: H.C. is inventor of several patents related to organoid technology, is cofounder of Xilis Inc. and is currently employee of Roche, Basel (CH) Switzerland. His full disclosure is given at https://www.uu.nl/staff/JCClevers/.

[1]M.B., M.H.G., and S.G. contributed equally to this work.

[2]To whom correspondence may be addressed. Email: h.clevers@hubrecht.eu.

[3]Present address: Roche Pharmaceutical Research and Early Development, Basel 4070, Switzerland.

This article contains supporting information online at https://www.pnas.org/lookup/suppl/doi:10.1073/pnas.2309902121/-/DCSupplemental.

Published March 14, 2024.

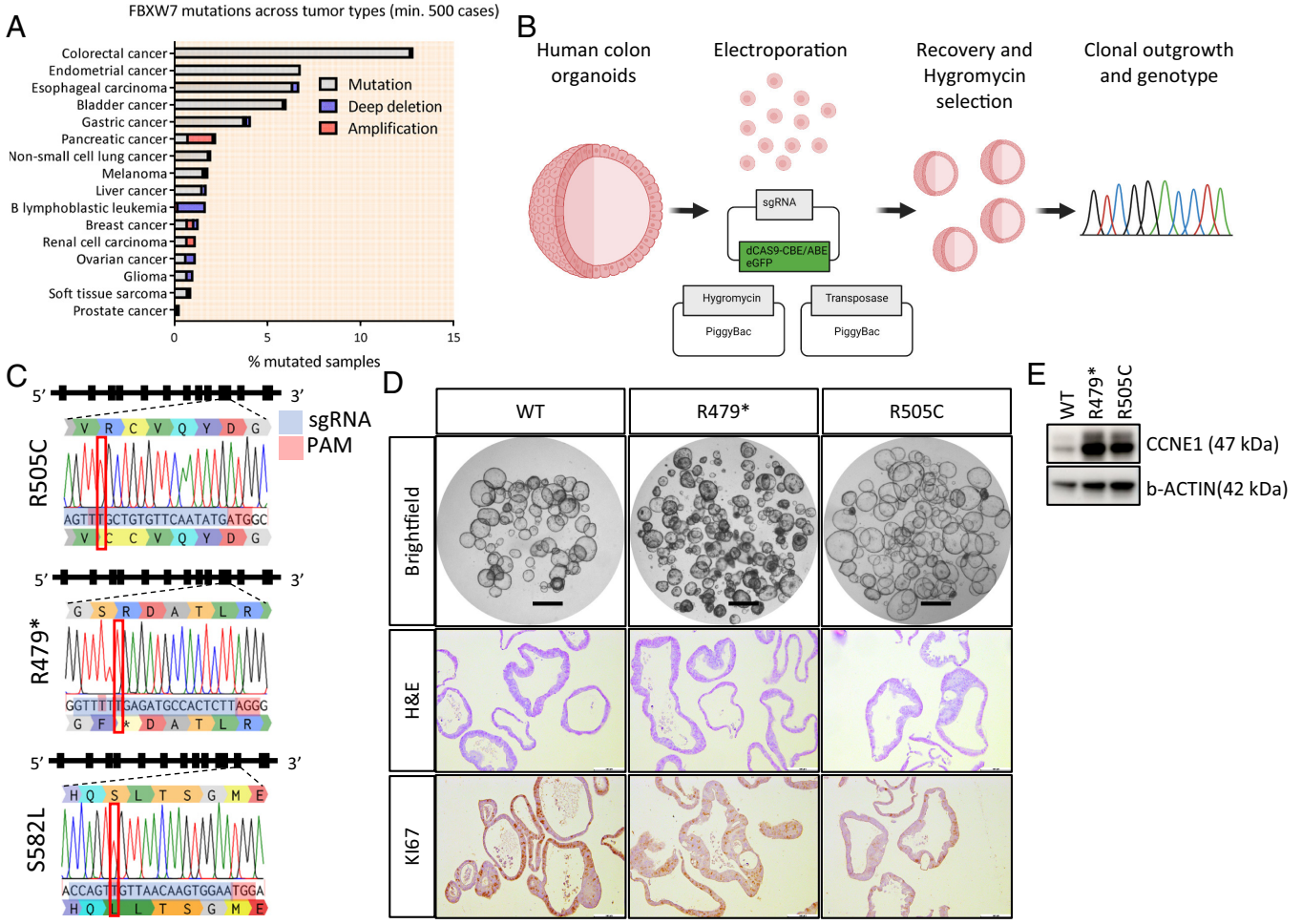

Fig. 1. Establishment of *FBXW7* mutant colon organoids. (*A*) Bar graph displaying the incidence of *FBXW7* mutations across different tumor types with at least 500 cases (systematic analysis of all cases reported in Cell BioPortal). (*B*) Descriptive flowchart of the experimental setup. (*C*) DNA traces of hotspot mutations introduced in colon organoids; the original aa sequence of the locus is reported above the DNA traces while the changed aa is reported below. PAM and sgRNA sequences are reported in red and blue, respectively, the red box indicates the desired mutation. (*D*) Representative bright-field and histological pictures of *FBXW7*-WT and mutant organoids. (Scale bar: 100 μm.) (*E*) Western blot showing the expression of CCNE1.

nucleotide changes of key arginine (Arg) amino acids (*SI Appendix*, Fig. S1*A*) within the substrate recognition (WD40) domain (*SI Appendix*, Fig. S1*B*) which inactivates one allele. Nevertheless, a second hit is often observed for those mutations which do not completely disrupt the substrate recognition domain and for truncating mutations. Furthermore, according to the COSMIC database, colon and endometrial cancer cases have been reported to contain homozygous FBXW7 hotspot missense mutations as well (R465C, R479Q, and R505C), while their frequency appears more common in acute lymphoblastic T cell leukemia. As most of these mutations represent C > T or A > G transitions, this allowed us to employ cytosine and adenine base editors (CBE and ABE) (40–44) to introduce individual *FBXW7* hotspot mutations in hCOs and thus to investigate their effect in CRC. In the absence of an efficient growth factor-based selection strategy, we used the optimized PiggyBac transposon system (45, 46) (which carries a hygromycin B resistance cassette) to select for electroporated organoids (47). Next, we individually picked clonal organoids and genotyped these to confirm the presence of the intended mutations (Fig. 1*B* and *SI Appendix*, Fig. S1*C*). This strategy allowed us to successfully introduce the following mutations: R278*, R479*, R479Q, R505C, Y545C, S582L, and R689W. Of note, R479 and R505 represent the most common mutational *FBXW7* targets in CRC. We thus established a mini-biobank of *FBXW7* mutant hCOs (Fig. 1*C* and *SI Appendix*, Fig. S1 *D* and *E*). We analyzed editing efficiencies of individual sgRNAs in different donors and observed variation depending on the sequence of the PAM or the sgRNA as well as the base editor employed, in agreement with previous reports (*SI Appendix*, Fig. S1*E*) (48). To exclude mitigating effects from the WT allele on our phenotypes, we focused on homozygous (HOM) mutant organoids for our analyses. *FBXW7* mRNA expression levels of the different *FBXW7* mutants were comparable to those of WT hCOs (*SI Appendix*, Fig. S1*F*) except for the R479* mutation, which appeared to undergo nonsense-mediated mRNA decay.

FBXW7-mutant organoids retained the cystic morphology and proliferative potential of WT organoids upon in vitro propagation (Fig. 1*D*) in complete expansion medium. Protein levels of CCNE1, a well-established FBXW7 target known to accumulate in mutant cells (14, 20), were up-regulated in organoids carrying common missense or nonsense mutations (Fig. 1*E*) supporting the successful disruption of FBXW7 in our engineered hCOs.

***FBXW7* Mutations Reduce EGF Dependency in hCOs.** Colon cancer develops through a sequence of driver mutations (49) that hijack signaling by essential stem cell growth factor cascades (38, 50). Notably, the Wnt and EGF signaling cascade are typically mutationally activated while the BMP pathway is blocked. In its simplest form, a given mutation might alter the dependency on a specific signaling pathway, which is reflected by the ability of

organoids to propagate in the absence or reduced presence of the pertinent growth factor (38, 50, 51). We therefore investigated the effects of *FBXW7* mutations toward niche factor dependency. We dissociated hCOs into single cells and cultured these in the absence of key factors of the hCO medium (i.e., Wnt/Rspondin1, the BMP inhibitor Noggin, EGF) (*SI Appendix*, Fig. S2*A*) and monitored organoid formation and expansion. Each individual growth factor remained essential for continued growth (*SI Appendix*, Fig. S2*B*), as determined by the inability of the organoids to grow in their absence. Yet, in medium lacking EGF, *FBXW7* mutant organoids showed a higher viability and clonogenic potential compared to WT (*SI Appendix*, Fig. S2*C*). We therefore tested whether *FBXW7* mutations reduced the dependency on EGFR activation by titrating EGF in the organoid culture medium. Indeed, organoids harboring mutations within the WD40 domain retained the potential to propagate indefinitely with as low as 5 pg/mL of EGF with a relatively constant splitting dynamics (Fig. 2 *A* and *B* and *SI Appendix*, Fig. S2*D*). Since WT organoids require 50 ng/mL of EGF, the mutant organoids showed a 10,000-fold reduction in EGF dependency. Yet, they did not become fully independent of EGFR signaling (Fig. 2*A*). This reduced EGF dependency was confirmed by analysis of the proliferation marker Ki67 which showed significant differences between WT and mutant organoids upon titration of the mitogen (Fig. 2 *C* and *D*).

Interestingly, not all mutations affecting the substrate recognition domain yielded a comparable phenotype. The SNV R689W, despite being frequently observed in CRC (*SI Appendix*, Fig. S1*A*), did not resemble the R479* or the R505C (which affect key Arg amino acids for the interaction with the substrates) (13) in terms of EGF dependency. Indeed, the C-terminal R689W mutation, in the last exon of *FBXW7*, behaved comparably to WT.

To further investigate whether the organoids could sustain EGFR activity, we cultured our organoids for 7 d and then removed EGF for 24 h and performed RNA sequencing. This analysis revealed upregulation of target genes of EGFR/MAPK activity such as *DUSP5*, *ETV4/5*, *E2F1*, *APOD*, *AREG*, and *EREG* in R505C

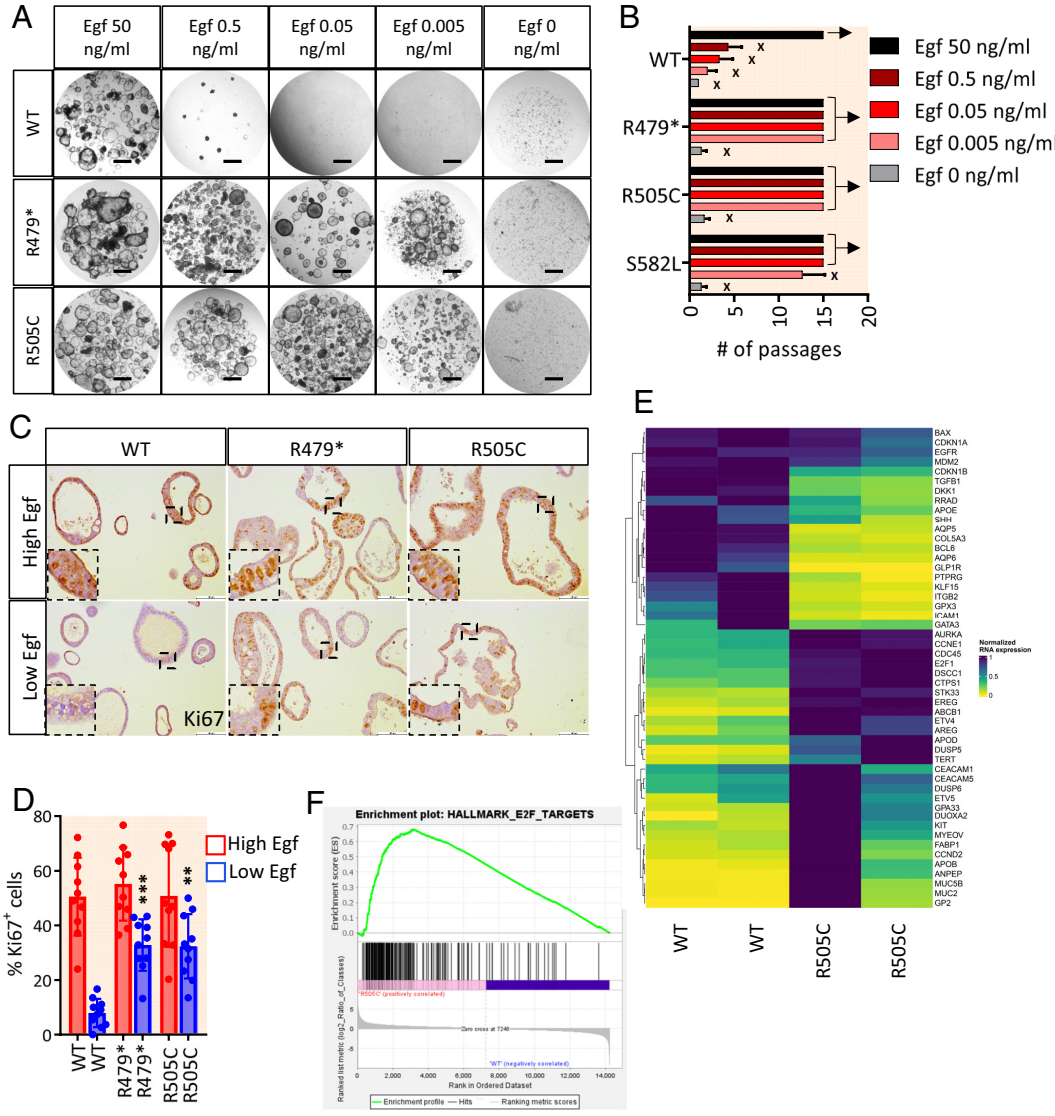

Fig. 2. FBXW7 mutations reduce the Egf dependency in human colon organoids. (*A*) Representative bright-field pictures of FBXW7 WT and mutant colon organoids cultured in the presence of different concentrations of Egf. (Scale bar: 100 µm.) (*B*) Bar graph showing the expansion potential of the organoids in different Egf concentrations (arrows indicate continued growth, x indicates the absence of growth). (*C*) Representative pictures of Ki67 staining on FBXW7 WT and mutant organoids cultured in high (50 ng/mL) and low Egf (0.5 ng/mL). The *Insets* show higher magnification of cell nuclei. (Scale bar: 100 µm.) (*D*) Bar graph summarizing the ki67 quantification in high and low Egf, n = 10, ** stands for *P*-value < 0.01, ***P-value < 0.001 vs. WT in low Egf; (*E*) Heatmap showing the expression of MAPK target genes between WT and mutant organoids. Genes have been extracted from the differentially regulated ones showing a Log2 FC > 1.5. Colors range from low (yellow) to high (dark blue) reads count. (*F*) GSEA showing increased activity of proliferative E2F target genes in FBXW7 mutant organoids.

mutant organoids (Fig. 2*E* and Dataset S1) as compared to WT organoids. Mutant organoids exhibited a slightly higher MPAS score compared to WT organoids suggesting higher residual activity of the MAPK pathway (0.3 and 0.2, respectively). The MPAS score has been validated as an approach to determine the activation status of the MAPK pathway; higher scores correlate with increased pathway activity and poorer overall survival in metastatic CRC. To further extend our analysis by investigating global transcriptomic changes, we performed Gene Set Enrichment Analysis (GSEA) which corroborated the increased proliferative activity through the MAPK pathway as well as enhanced KRAS signaling, inducing E2F target gene expression (Fig. 2*F* and *SI Appendix*, Fig. S2*E*). We next assessed the expression of a selected list of MAPK target genes in different FBXW7 mutant organoids upon EGF withdrawal and found these to be up-regulated in comparison to WT organoids with the R505C mutants showing the strongest phenotype (*SI Appendix*, Fig. S2*F*). Interestingly, we noted increased expression of EGF-like ligands such as *AREG*, *EREG,* and *NRG1* in FBXW7^{R505C} hCOs in our RNA sequencing (Fig. 2*E* and *SI Appendix*, Fig. S2*G*). Such ligands possess an EGF-like domain that allow interaction with EGFR and other members of the ERBB family (i.e., ERBB2/3/4) (52).

To exclude the possibility that the increased proliferation of mutant organoids in limited EGF concentration was due to increased production of these endogenous RTK ligands, we investigated the rescuing effect of such ligands in WT organoids cultured with 5 pg/mL of EGF. Despite some initial growth, we could not establish long-term expanding organoid cultures (*SI Appendix*, Fig. S2*H*) which supported our conclusion that the ability of *FBXW7* mutant organoids to propagate in the limited presence of mitogens is not due to their increased endogenous production but rather appeared related to enhanced activation of the EGFR/MAPK axis.

EGFR Protein Is Stabilized upon*FBXW7* Mutation. To further understand the relation between FBXW7 mutations and signaling through the EGFR, we used our engineered hCOs which were cultured with 0.5 ng/ml EGF for a week before analysis. As expected, ligand binding led to clearance of the receptor from the cellular membrane of WT cells. By contrast, EGFR accumulated in *FBXW7*-mutant hCOs as observed by western blot analysis (Fig. 3*A*). Also, CCNE1 accumulated in R505C mutant organoids, supporting the robustness of the phenotype (Fig. 3*B*). This effect was not due to increased EGFR gene expression as evidenced by the unaltered read count between FBXW7 WT and R505C mutant organoids detected in our RNA sequencing data (Fig. 2*E* and *SI Appendix*, Figs. S2*G* and S3*A*).

We next performed whole-mount staining on hCOs to investigate the localization of the receptor. We cultured our organoids for 5 d in the presence of EGF and then removed EGF for two additional days. Clear membrane signaling was detected in *FBXW7* mutant but not WT organoids (Fig. 3*C*). To further understand how different *FBXW7* mutations might impact EGFR stabilization, we used our mini-biobank of *FBXW7* mutant hCOs and performed fluorescent staining using Cetuximab 647-conjugated EGFR antibody as a readout of EGFR expression at the cell membrane. We therefore cultured our organoids for a week with EGF (i.e., 0.5 ng/mL) and then stained EGFR. Live imaging of the organoids showed a clear membrane pattern, reflecting efficient binding with membranous EGFR (*SI Appendix*, Fig. S3*B*). Subsequent FACS analysis determined the intensity of the membrane signal. This showed variations among different mutations with the most intense staining peaking at R479*/Q and R505C variants (Fig. 3 *D* and *E*). As expected, R689W mutant hCOs did not show significant changes when compared to WT organoids.

***FBXW7* Mutant hCOs Require EGFR Engagement for Efficient Growth.** Mutant hCOs required activation of EGFR for long-term propagation in vitro (Fig. 2*A*). We next investigated whether the effects observed in *FBXW7* mutant organoid were dependent on efficient engagement of the EGFR. We thus assessed the growth of hCOs in the presence of different RTK ligands and evaluated their viability after 7 d of culture and long-term propagation by passaging. Addition of ligands of ERBB family members (Nrg1, Ereg, Areg, Hrg-β1, and Tgf-α) could partially rescue the absence of EGF during initial wt organoid formation. However, no effect was observed long term (Fig. 3 *F* and *G* and *SI Appendix*, Fig. S3*C*). Similarly, Fgf2, Fgf10, and Igf1 could sustain initial organoid formation but were inefficient mitogens after just a few passages (Fig. 3*G* and *SI Appendix*, Fig. S3*C*) as previously reported (53). Importantly, FBXW7 R479/505 mutant organoids could be rescued by ERBB ligands that directly or indirectly recruit EGFR (52) (Areg, Ereg, and Nrg1) while failing to propagate in the presence of other TRK activators (Fig. 3 *F* and *G* and *SI Appendix*, Fig. S3*C*). In particular, FBXW7^{R505C} organoids successfully replicated in vitro at similar dynamics when stimulated with EGF or with EGF-like ligands AREG, EREG, and NRG1. These results showed that *FBXW7* mutant organoids remain dependent on EGFR recruitment for efficient growth, be it by EGF or by EGF-like ligands. Next, we investigated the effect of EGF supplementation to the activation of the EGFR/MAPK pathway in our hCOs. For this, we cultured hCOs and removed EGF from the medium for 48 h (to deplete downstream signaling), followed by EGFR reactivation by EGF supplementation. We then measured MAPK activity after 6 h through the expression of MPAS-related target genes. As expected, we found higher expression of key early target genes of ERK activation (DUSP5, DUSP6, EPHA4, and SPRY4). Of note, we did not detect a higher expression of some other target genes like ETV4 and ETV5, possibly due to higher baseline expression in mutant organoids upon EGF depletion compared to WT which allows mutant organoids to partially sustain the activity of the MAPK pathway in a limiting EGF concentration (*SI Appendix*, Fig. S3*D*).

Proteomic Analyses Support EGFR Stabilization upon FBXW7 Mutation. FBXW7 targets phosphorylated proteins for ubiquitin-dependent degradation by the proteasome. We cultured hCOs in low EGF and performed quantitative mass spectrometry to assess the accumulation of ubiquitinated and phosphorylated proteins (*SI Appendix*, Fig. S3*E*). We found a total of 1,628 proteins with lower ubiquitylation in the mutant cells (Dataset S2) confirming loss of E3 ligase activity and the dysregulation of polyubiquitylation and ubiquitin-dependent catabolic processes (*SI Appendix*, Fig. S3*F*). Among several candidates, we identified previously FBXW7 targets like MYC, MCL1, and STAT3 and confirmed loss of ubiquitylation of the EGFR (*SI Appendix*, Fig. S3*G* and Dataset S2). We next performed quantitative mass spectrometry to discriminate enriched proteins in mutant cells, generating a list of 269 hits which accumulated with spectral counts >twofold in mutant organoids (*SI Appendix*, Fig. S3*H* and Dataset S3). Among the accumulated proteins, we detected a >twofold increase in EGFR abundancy in FBXW7 mutant organoids (*SI Appendix*, Fig. S3 *H* and *I*).

FBXW7 targets substrates which have been previously phosphorylated at Thr or Ser amino acids within CPD motifs. We next cultured mutant and WT hCOs in low EGF for 7 d and then performed proteomic analysis on phosphorylated proteins. We identified 1,526 phosphopeptides with at least a twofold increase in FBXW7 mutant organoids (Dataset S4). Among the targets, we detected ~fourfold increase of two distinct phosphopeptides

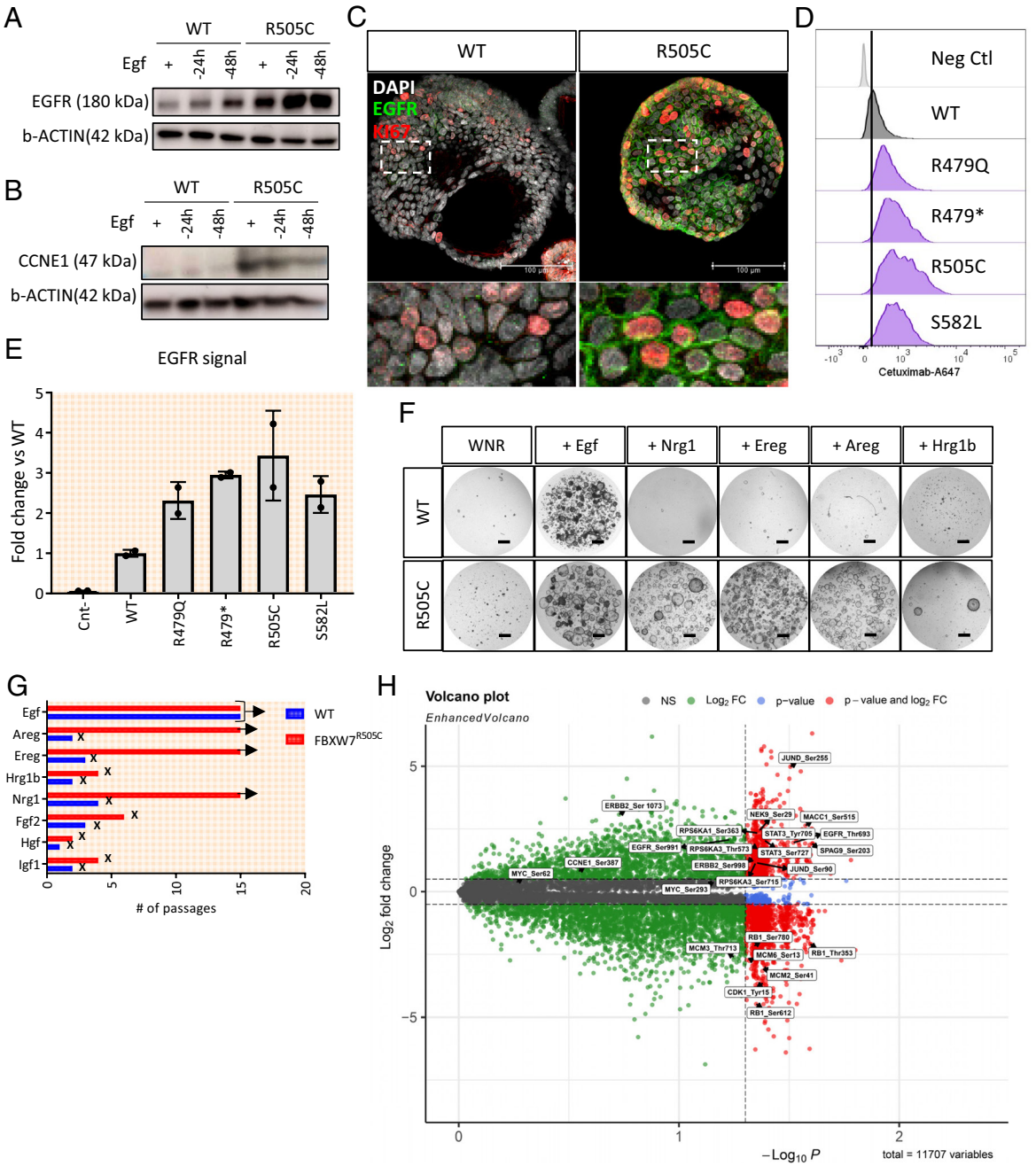

Fig. 3. Impact of FBXW7 mutations on EGFR. (*A* and *B*) Western blot showing differential expression of EGFR (*A*) and CCNE1 (*B*) in FBXW7 WT and mutant organoids cultured in the presence of 0.5 ng/mL of Egf and after it has been removed for 24 h and 48 h. (*C*) Whole-mount staining for EGFR and KI67. (Scale bar: 100 μm.) (*D*) FACS plot showing increased cell membrane localization of EGFR in FBXW7 WT and mutant organoids, n = 2. (*E*) Bar graph reporting the quantification of EGF intensity at the cell membrane in different FBXW7 mutant as measured by FACS with a Cetuximab-647 antibody, n = 2. (*F* and *G*) Bright-field pictures of WT and mutant organoids cultured in the presence of different ERBBs activators, scale bar 100 μm (*F*) and quantification of their ability to propagate in vitro in the presence of the indicated growth factor (*G*) (arrows indicate continued growth, x indicate the absence of growth). (*H*) Volcano plot highlighting the enrichment of phosphorylated proteins between WT and FBXW7 mutant organoids, n = 3.

of the EGFR with phosphodegron-like characteristics (i.e., Thr693 and Ser991) (Fig. 3*H* and *SI Appendix*, Fig. S3 *J* and *K*). Previous known targets like JUN, STAT3, CCNE1, CCNL1, and MYC were also detected (Dataset S4).

Together, our combined ubiquitome and total proteome analyses implied that EGFR protein is stabilized upon *FBXW7* mutations.

FBXW7 Degron-Like Motifs in the EGFR. E3 ligase interaction with their substrates depends on a short amino acid sequence, known as phosphodegron, within the target protein which is recognized and bound by the enzyme complex responsible for the conjugation of the ubiquitin moieties (8, 9). FBXW7 has been shown to bind two distinct CPDs defined by a central phosphorylated S or T at position 0 (*SI Appendix*, Fig. S4*A*). CPD motif one consists of two phosphorylated S at position 0 and +4, respectively, while CPD motif two consists of a central phosphorylated T at position 0 followed by a phospho-mimicking amino acid at position +4. In either case, the central phosphorylation site is followed by a mandatory proline and preceded by a hydrophobic pocket at position −1/2 (13). Based on the accumulation of EGFR observed in our *FBXW7* mutant organoids, we analyzed EGFR amino acid sequence and identified at least three possible CPDs at T693, S991, and S1026, respectively (Fig. 4*A*). These CPD-like motifs span the juxta membrane and protein tyrosine kinase domains of

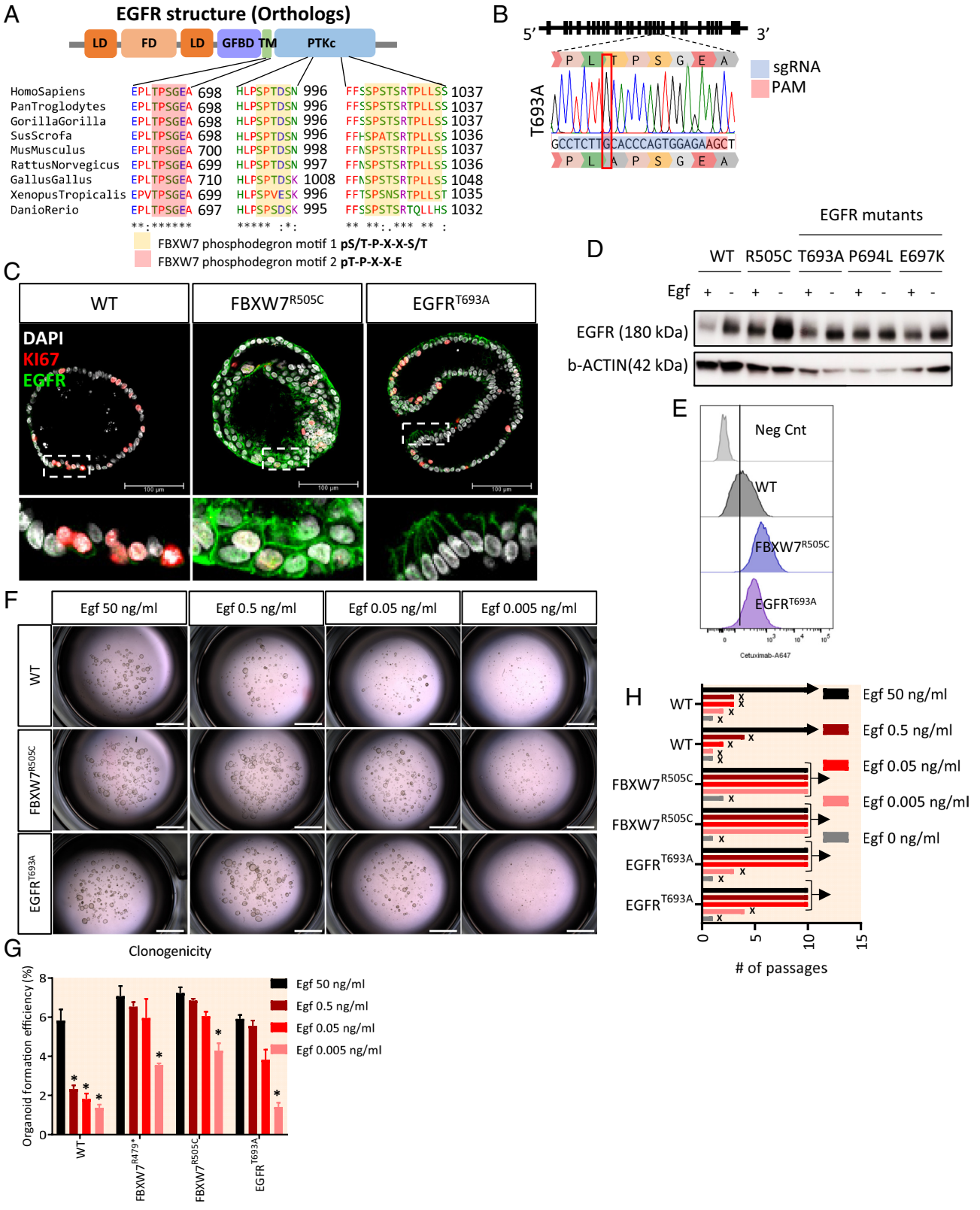

Fig. 4. EGFR contains two phosphodegron sites. (*A*) Alignment of the EGFR sequence among orthologs showing the conserved presence of multiple phosphodegron-like motifs. (*B*) DNA traces of T693A mutation; the original aa sequence of the locus is reported above the DNA traces while the changed aa is reported below. PAM and sgRNA sequences are reported in red and blue, respectively. (*C*) Whole-mount staining of EGFR in EGFR WT and mutant organoids. (Scale bar: 100 µm.) (*D*) Western blot showing EGFR expression in WT and EGFR mutant organoids. (*E*) FACS plot showing the expression of membrane-bound EGFR in WT and phosphodegron mutant organoids. (*F* and *G*) Bright-field pictures (*F*) and quantification (*G*) of the clonal outgrowth of WT and phosphodegron mutant organoids in limiting Egf concentrations, * stands for *P*-value < 0.05. (*H*) Bar graph showing the long-term culture potential of WT, FBXW7 and EGFR degron mutant organoids (arrows indicate continued growth, and x indicates the absence of growth), results from two individual clones are represented in the bar graph.

EGFR. Disruption of CPD motifs is a known mechanism that can impair FBXW7 binding and stabilize its substrate (8, 9). Consequently, we used CRISPR base editors to introduce specific mutations in EGFR CPDs. We initially focused on the T693 CPD which is involved in the negative regulation of EGFR signaling (54, 55) and contained only one phosphor site. We introduced T693A, P694L, and E697K mutations in EGFR to specifically change the central phosphorylated amino acid, the mandatory proline, and the phosphor-mimicking glutamic acid at position +4 (Fig. 4*B* and *SI Appendix*, Fig. S4 *B–D*).

To understand whether we could stabilize EGFR by mutating its potential CPDs, we used whole-mount staining to visualize the expression level of the receptor. As reported above, EGFR is not detectable in WT hCOs because of efficient clearance from the membrane in the presence of EGF, a phenomenon which is impaired in *FBXW7* mutant organoids. When staining $EGFR^{T693A}$ mutants, we detected a clear membrane signal which was confirmed by western blot and FACS analysis (Fig. 4 *C–E* and *SI Appendix*, Fig. S4*E*). This confirmed EGFR accumulation relative to WT organoids. Interestingly, the intensity of EGFR in T693A organoids was halfway between *FBXW7* mutant and WT organoids, suggesting that mutation of just one CPD might not be sufficient to completely disrupt the interaction with the E3 ligase (as previously reported for other substrates) (12, 15). Importantly, mutations affecting the EGFR phosphodegron are observed in human cancer, particularly of the lung which is burdened by a relatively low *FBXW7* mutational rate (~2%) and high *EGFR* mutational rate (~26%). In particular, mutations at T693 (producing the T693A) and mandatory P694 (inducing the P694L and P694S) as well as mutations changing the hydrophobic pocket upstream to the central phosphosite have been reported (Dataset S5).

$EGFR^{T693A}$ hCOs Require Less EGF for Efficient Propagation. To understand how the $EGFR^{T693A}$ mutation within the putative CPD domain affects EGF-mediated signaling, we performed clonogenicity experiments by seeding 5,000 single cells in decreasing concentrations of EGF and counting formed organoids 8 d later. As expected, decreasing EGF concentration severely impacted organoid formation efficiency of WT organoids while only moderately affected *FBXW7* mutant hCOs when cultured with 5 pg/mL Egf (Fig. 4 *F* and *G*). Importantly, $EGFR^{T693A}$ cells were only significantly affected in the lower concentrations and showed effective clonogenicity with as low as 50 pg/mL of Egf (Fig. 4 *F* and *G*). We also assessed the doubling time of WT and mutant cells by counting cells every 48 h for 8 d. In WT cells, the doubling time was affected already at 0.5 ng/mL of Egf (near physiological concentration) as compared to *FBXW7* mutant organoids. In $EGFR^{T693A}$ hCOs, we noted a significant reduction in cell proliferation only at the lowest EGF concentration (i.e., 5 pg/mL) (*SI Appendix*, Fig. S4*F*). As confirmation, we successfully expanded $EGFR^{T693A}$ organoids at constant splitting ratio in as low as 50 pg/ml of EGF for at least 10 passages after which the experiment was stopped (Fig. 4*H* and *SI Appendix*, Fig. S4 *G* and *H*). As EGF-like ligands could rescue *FBXW7* mutant organoids from the absence of EGF (Fig. 3 *F* and *G*), we cultured hCOs with the EGF-like ligands Areg, Ereg, or Nrg1 as replacement of EGF. As observed for the $FBXW7^{R505C}$ mutants, $EGFR^{T693A}$ organoids could propagate in the presence of either ligand (*SI Appendix*, Fig. S4*H*).

***FBXW7* Mutant Organoids Show Altered Response to Inhibitors of the EGFR/MAPK Pathway.** The first line of treatment for a metastatic CRC normally relies on the combination of different chemotherapeutic agents. When unsuccessful, the second-line treatment option aims at targeting receptors crucial for tumor growth, limiting blood supply or mitogenic stimuli for tumor cells. Cetuximab and Panitumumab, which inhibits EGFR by binding to its extracellular domain, are second-line treatment options for metastatic *KRAS*/*BRAF* WT CRC. *FBXW7* mutations have been previously associated with reduced sensitivity toward inhibitors of the EGFR in the clinics (34–36, 56, 57). Nevertheless, high EGFR expression has been shown to predict sensitivity to Cetuximab as well as higher mRNA expression of the Egf-like ligands *AREG* and *EREG* leading to a dependence on the activation of the EGFR (58, 59), corroborated in our engineered hCOs by EGFR activation-dependent growth.

To elucidate the impact of FBXW7 mutations on the response to inhibitors of the EGFR/MAPK pathway, we performed a drug screening of our mini-biobank of mutant hCOs with multiple inhibitors (*SI Appendix*, Fig. S5*A*). We first standardized our drug screening assay by testing the second-generation EGFR inhibitor Afatinib on hCOs engineered with a $KRAS^{G12D}$ mutation and compared the response with that of WT organoids, determining the concentration range and the average response for sensitive and resistant lines (*SI Appendix*, Fig. S5 *B* and *C*). Next, we analyzed the *FBXW7* mutant hCOs. Differential responses were observed depending on the specific mutations that were introduced (*SI Appendix*, Fig. S5 *D–F*). As expected, WT hCOs relied on active EGFR signaling as even in the presence of minimal dosage of the irreversible inhibitor the viability was greatly reduced. Conversely, *FBXW7* mutant hCOs showed a general trend toward drug resistance. Mutations affecting exon 10 (i.e., R479Q/*, R505C) showed stronger resistance than mutations affecting later exons (*SI Appendix*, Fig. S5 *E* and *F*).

Treatment of metastatic CRC mainly relies on use of monoclonal antibodies targeting the ligand-binding domain of the EGFR such as Cetuximab. We thus treated our hCOs with increasing concentrations of Cetuximab and observed similar results, with the $FBXW7^{R505C}$ mutant organoids showing the lowest response (Fig. 5 *A–C*).

CRC-Derived Organoids with *FBXW7* Mutations Showed Reduced Sensitivity to EGFR Inhibitors. CRC-derived organoids have been shown to maintain key features of the primary tumor and been amenable to drug screening (60, 61). We next screened our previously assembled collection of 69 CRC-derived organoids and found four samples with *FBXW7* mutations but no other alteration of the MAPK pathway (Dataset S6). We then assessed the response of these organoids to Afatinib (*SI Appendix*, Fig. S5 *D*, *G*, and *F*) and Cetuximab (Fig. 5 *D* and *E*) and compared this to *FBXW7* WT CRC organoids and WT hCOs. Overall, we observed a significant difference of response between WT and mutant CRC organoids, with the latter displaying higher IC50s. A similar trend was observed for the MEKi Trametinib (Fig. 5*E* and *SI Appendix*, Fig. S5*H*).

Clinical Response to EGFR Inhibition in *FBXW7* WT and Mutant CRC Patients. To better understand the impact of these mutations on the response to EGFR-targeted therapy of metastatic CRC patients, we collected response data from 11 *FBXW7* mutant and 51 *FBXW7* WT patients treated with Panitumumab or Cetuximab, two EGF-competing antibodies, and compared their response to therapy (Dataset S7).

Of note, patients with KRAS and BRAF mutations were excluded from the cohort in agreement with current stratification methods (62). We then investigated the percentage of patients in both groups who progressed through the treatment at the end point. We observed that while 80% of *FBXW7* WT patients showed disease progression, 100% of mutant patients showed progressive disease upon anti-EGFR treatment (*SI Appendix*, Fig. S5*I*).

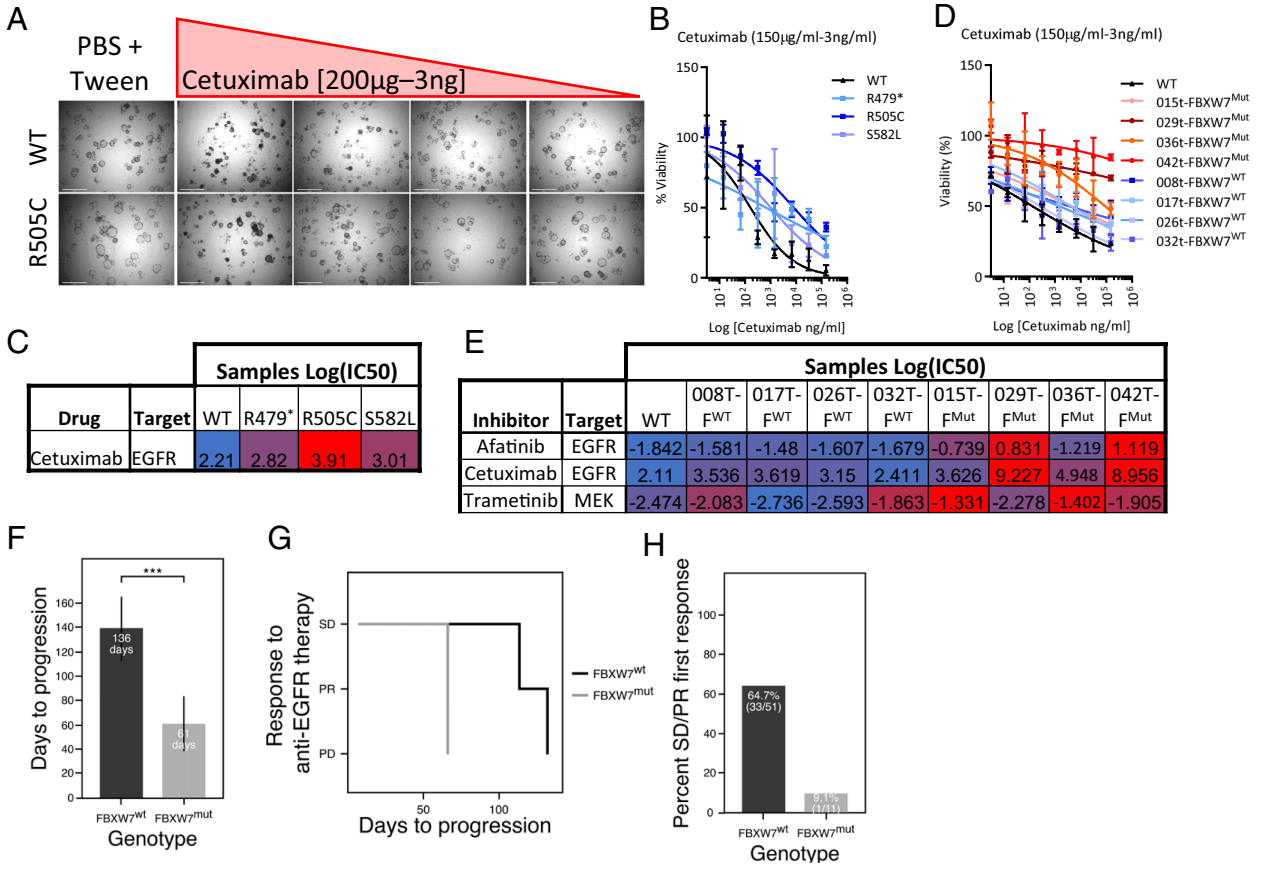

C

Drug	Target	Samples Log(IC50) WT	R479*	R505C	S582L
Cetuximab	EGFR	2.21	2.82	3.91	3.01

E

Inhibitor	Target	Samples Log(IC50) WT	008T-FWT	017T-FWT	026T-FWT	032T-FWT	015T-FMut	029T-FMut	036T-FMut	042T-FMut
Afatinib	EGFR	-1.842	-1.581	-1.48	-1.607	-1.679	-0.739	0.831	-1.219	1.119
Cetuximab	EGFR	2.11	3.536	3.619	3.15	2.411	3.626	9.227	4.948	8.956
Trametinib	MEK	-2.474	-2.083	-2.736	-2.593	-1.863	-1.331	-2.278	-1.402	-1.905

Fig. 5. FBXW7 mutations reduce the sensitivity toward anti-EGFR therapies. (*A*) Bright-field pictures of FBXW7 WT and mutant organoids treated with decreasing concentrations of Cetuximab. (Scale bar: 500 µm.) (*B*) Dose–response curve indicating the Cetuximab sensitivity of different organoid lines. (*C*) Heatmap indicating the IC50s of Cetuximab on FBXW7 WT and mutant lines. (*D*) Dose–response curves indicating the sensitivity to Cetuximab of FBXW7 WT and mutant CRC-derived organoids. (*E*) Heatmap indicating the IC50s of different inhibitors tested on CRC-derived FBXW7 WT and mutant lines, color range from low (blue) to high (red) IC50. (*F*) Bar graph showing the number of days required to progress in our patients' cohort. (*G*) Kaplan–Meier survival analysis describing the faster progression of FBXW7-Mutant patients treated with the anti-EGFR treatment. (*H*) Bar graph showing the percentage of patients showing SD or PR as the first response to treatment with anti-EGFR antibodies; SD, PR, and PD represent stable disease, partial response, and progressive disease, respectively.

Among those patients who progressed, time to progression was shorter for *FBXW7* mutant patients (61 d) than *FBXW7* WT patients (137 d) (Fig. 5 *F* and *G*). Importantly, only one *FBXW7* mutant patient (9,1%) reached stable disease. This is in stark contrast with FBXW7 WT patients where 33 out 51 (64,6%) manifested an initial stable disease or even partial response before showing disease progression (Fig. 5*H*). Remarkably, while all of the FBXW7 mutant patients progressed within the first 4 mo of treatment, 52,3% of FBXW7 WT patients (23/44) still presented a stable disease or partial response (*SI Appendix*, Fig. S5*J*).

Taken together, our data showed that while mutant cells still require EGFR activation for their efficient growth, *FBXW7* mutations such as those observed in CRC might reduce the efficacy of anti-EGFR therapies.

Discussion

Here, we use a combined approach based on targeted mutagenesis, proteomic, and transcriptomic analyses to investigate the effects of *FBXW7* mutations in human colon organoids. Previous studies have relied on the use of immortalized, carcinoma-derived cell lines which have led to the identification of a plethora of targets (10, 14, 16–18, 21, 31). We opted for a near-physiological human experimental platform: wild-type human colon organoids which have been shown to maintain genomic stability and physiology during long-term propagation (37). We generated a biobank representative of the most common *FBXW7* mutations in CRC: R278*, R479*, R479Q, R505C, Y545C, S582L, and R689W. Functional phenotyping of these mutant lines demonstrated a 10,000-fold reduced dependence on EGF for efficient propagation. The severity of this phenotype differed depending on the mutational event, suggesting that C-terminal mutations in *FBXW7* do not completely disturb E3 ligase activity. We thus identified EGFR as a target of FBXW7. By combining different approaches, we validated the accumulation of EGFR in mutant organoids in the presence and absence of (near) physiological concentrations of EGF in our medium.

RNA sequencing analysis revealed that EGFR gene transcription is unaltered, implying the accumulation to be a consequence of protein stabilization through impaired degradation. Proteomic analyses revealed stabilization of the EGFR in FBXW7 mutant organoids through reduced ubiquitylation of the phosphorylated receptor. Analysis of the EGFR sequence predicted the presence of several CPD-like motifs. Of interest, mutations of these CPD-like motifs were found in cancer, most notably of the lung (COSMIC database). Indeed, the T693A mutation allowed EGFR accumulation while reducing EGF dependency in a similar way as did *FBXW7* mutations. This implies that these phosphodegron-targeting point mutations in EGFR contribute to malignant transformation. Of note, the introduced phosphodegron mutations were less potent than the FBXW7 mutations in terms of relieving EGF dependency. This divergence is possibly explained by redundancy

with the remaining CPDs on the EGFR which could still allow interaction with FBXW7. Indeed, dimerization of the E3 ligase has been demonstrated to improve target binding and degradation through the presence of multiple CPDs on target proteins so that disrupting one CPD alone only partially impairs target ubiquitination (11–13, 15).

When we analyzed a clinical cohort, we found that *FBXW7* mutant metastatic CRC fared worse than WT patients when treated with the EGFR inhibitor Panitumumab or Cetuximab, both in terms of the percentage of patients who progressed through the disease and the time needed for progression. Previous studies have hinted at the presence of *FBXW7* mutations among tumor patients resistant to anti-EGFR therapies (34, 56, 57), and our data are in agreement with this notion. Thus, *FBXW7*mutational status might be a parameter that should be taken into account when targeting the EGFR pathway in cancer.

Materials and Methods

Organoid Cultures. Human colon organoids were used for the experiments described in this manuscript. The organoids were expanded as previously described (40) in a medium containing R-Spondin conditioned medium (10%, home-made), Wnt surrogate (1:1,000 Wnt surrogate, U-Protein Express) Noggin conditioned medium (1%, U-Protein Express), B27 (2%,), n-Acetyl Cysteine (1,25 mM, Sigma), Nicotinamide (10 mM, Sigma), A83-01 (500 nM, Tocris), p38 inhibitor SB202190 (3 μM, Sigma), human EGF (50 ng/ml, PeproTech), Prostaglandin E2 (10 nM, Tocris), Rho kinase inhibitor Y-27632 dihydrochloride (10 μM, Abmole Bioscience), and Primocin (100 μg/mL, InvivoGen) supplemented in basic culture medium consisting of Advanced Dulbecco's modified Eagle's medium (DMEM)/F12 with B27, GlutaMAX, HEPES, and penicillin/streptomycin (Thermo Fisher). The medium was refreshed every 2 d and the organoids were weekly passaged by enzymatic dissociation. In brief, the organoids were removed from Cultrex Basement Membrane Extract (BME, Growth Factor Reduced, Type 2, R&D Systems) with ice-cold AdDMEM+++ and incubated with TrypLE (Thermo Fisher) for 3 min, washed with ice-cold AdDMEM+++, and replated in fresh BME.

The CRC-derived organoids used in this study were previously established and cultured as described above. The list of CRC organoid lines used in this study is reported in Dataset S6.

CRISPR-Mediated Gene Editing of Human Colon Organoids. CRISPR plasmids were generated as previously described, and the electroporation was performed according to published protocols (40, 47). In brief, the organoids were expanded for 4 to 5 d and switched to a medium containing Y-27632 48 h before the electroporation, while the day before 1.25% DMSO was added to the culture medium. On the day of the electroporation, the organoids were recovered from BME with ice-cold AdDMEM+++, digested to single cells with TrypLE 2 × 5′, washed with AdDMEM+++, and washed again in OptiMEM (Thermo Fisher). Finally, 1 × 10^6 cells were resuspended in 100 μL of OptiMEM containing 7.5 μg of GFP-expressing base editor (ABE or CBE, Addgene), 2.5 μg of sgRNA, 2 μg of hygromycin resistance-carrying piggyBac, and 6 μg of Transposase-carrying piggyBac. After the electroporation, the cells were allowed to recover at RT and then resuspended in BME and plated in prewarmed multiwell plates. GFP expression was monitored 24 h after electroporation, and hygromycin selection was started 5 to 6 d after.

The list of sgRNAs is reported in Dataset S8.

Establishment of Clonal Lines and Genotyping. After hygromycin selection, individual organoids were manually picked, dissociated, and replated in BME. Few days later, growing organoids were picked and genotyped to confirm the presence of the mutation. In brief, the DNA was extracted with the Quick-DNA Microprep Kit (Zymo Research) according to the manufacturer's instructions. Then, 5 to 10 ng of DNA was used for a PCR reaction with specific forward and reverse primers for an amplicon of 600 bp around the mutation site using the Phusion™ Plus DNA Polymerase (Thermo Fisher). The PCR products were purified with the NucleoSpin Gel and PCR CleanUp Mini Kit (Macherey-Nagel), and the cleanup products were sent for sanger sequencing with either the forward or reverse primer. The list of genotyping primers is provided in Dataset S9.

Growth Factors Screening Assays. Organoids cultured in expansion medium were digested to single cells, replated in BME in a 384-well plate at a density of 1,000 cells per well using a Multidrop Combi Reagent Dispenser (Thermo Scientific), and cultured in the presence of different TRK activators using the medium without EGF as basal medium. After 7 d, organoids viability was measured using Cell Titer Glo (CTG) and quantified with a Tecan spectrophotometer. The experiments were performed with four replicates and the results normalized to WNR condition. The ability of the organoids to expand in different media compositions was assessed by repeatedly passaging the organoids every 1 to 2 wk at constant splitting ratio (1:4) using TrypLE.

Organoid Formation Efficiency and Doubling Time. Organoids cultured in expansion medium were digested to single cells, replated in BME in a prewarmed 48-well plate at 5,000 cells per well density in 20 μL of BME drop, and cultured in different concentrations of EGF (i.e., 50 ng/mL, 0.5 ng/mL, 0.05 ng/mL, 0.005 ng/mL, and 0 ng/mL). After 7 d, the number of organoids was counted, and the organoid formation efficiency was calculated. To assess the doubling time, the organoids were recovered from BME and dissociated to single cells using TrypLE for 10′. Cells were counted using a hemocytometer every 48 h for 8 d. All experiments were performed in triplicates.

Western Blot. Organoids were collected from BME with ice-cold AdDMEM+++ and washed three times with ice-cold PBS(0). Total proteins were isolated with RIPA Buffer [50 mM Tris-HCl pH 8.0, 150 mM NaCl, 0.1% SDS, 0.5% Na-Deoxycholate, 1% NP-40, 1× Complete protease, and phosphatase inhibitors (Roche)], and protein concentration was measured using a BCA assay kit (Thermo Fisher). Fifty micrograms of total proteins was loaded on a precast gradient SDS-PAGE gel 12% (Bio-Rad) and subsequently transferred onto a PVDF membrane (Millipore). The membrane was blocked with 5% milk in PBST for 1 h prior to overnight incubation with the primary antibody. Antibodies used in this study are anti-EGFR (EP38Y #ab52894, Abcam), anti-Ubiquitin (P4D1 #3936, CST), anti-CCNE1 (HE12 #sc-247, Santa Cruz), and anti-β-Actin (HRP-conjugated 13E5, CST). Secondary antibodies used are swine anti-rabbit-HRP (Dako) and Rabbit anti-mouse-HRP (Dako). Membranes were imaged using the Amersham ImageQuant 800 western blot imaging system.

Immunohistochemistry Staining. Organoids were recovered from BME using Dispase (Sigma-Aldrich), fixed with 4% paraformaldehyde (PFA) for 1 h at room temperature, washed and dehydrated using an increasing ethanol gradient, and washed in xylene before embedding in paraffin. Paraffin sections were processed according to standard procedures. The following antibodies were used for stainings on paraffin sections, KI67 (B56 #550609, BD Pharmingen), according to the manufacturer's instructions. Slides were finally imaged using a Leica DM4000 microscope.

Whole-Mount Staining and Confocal Imaging. To perform whole-mount staining for the EGFR and better visualize the protein, the organoids were cultured for 5 d with EGF which was then removed for two additional days before they were collected for the analysis. The organoids were recovered from BME using Dispase and fixed in 4% PFA before being incubated in blocking buffer [PBS(0), 5%BSA, 0.1% Triton] for 1 h at RT. Primary antibody incubation was performed overnight at 4 °C followed by secondary antibody incubation for 3 h at RT light-protected. Following incubation with Dapi, the organoids were collected in permanent mounting medium (VectorLabs) and mounted on a slide which was imaged with a Leica Sp8 confocal microscope. Fluorescent images were processed for max projection of all z-stacks using ImageJ software. The following antibodies were used for whole-mount staining, EGFR (EP38Y #ab52894, Abcam), KI67 (B56 #550609, BD Pharmingen), Alexa-Fluor 488 donkey anti-rabbit (A21206, Life Technologies), and Alexa-Fluor 568 donkey anti-mouse (A10037, Life Technologies). The complete list of antibodies used is presented in Dataset S10.

Flow Cytometry. Organoids were expanded for 7 d in the presence of 0.5 ng/mL EGF before being used for the analysis. The organoids were then recovered from BME using Dispase and dissociated to single cells using TrypLE. Cells were then incubated with Cetuximab 647–conjugated (C225 Alexa-Fluor, R&D Systems) for 1 h on ice light-protected. Cells were washed twice in a buffer containing 5 mM EDTA. Cells were then filtered into FACS tubes through a cell strainer (Falcon), stained with Dapi to identify live cells (Sigma), and analyzed using the CytoFLEX benchtop flow cytometer (Beckman). Results were further interpreted with FlowJo

software. Fluorescent reporter gating strategy in human colon organoids is uniform across this study.

RNA Extraction and Real-Time PCR. Organoids cultured in different media composition were collected in lysis buffer. RNA extraction was performed with the RNeasy Mini Kit (Qiagen) following the manufacturer's instruction. One microgram of DNase-treated RNA was reverse transcribed into cDNA in a reaction with Oligo(dT)$_{15}$ Primer and GoScript™ Reverse Transcriptase kit (Promega). cDNA was then subjected to qPCR using iQ™ SYBR® Green Supermix (Bio-Rad) in the CFX Connect™ Real-Time PCR machine (Bio-Rad). Ct values of each gene were normalized to the housekeeping gene GAPDH (using the ΔCt method), and the relative expression of individual genes versus control conditions was then reported with the $2^{-\Delta\Delta Ct}$ method. The primers used in this study are as follows: *GAPDH* forward (gtctcctctgacttcaacagcg), reverse (aacaccctgttgctgtagccaa), *FBXW7* forward (tagaaccccagtttcaacgaga), reverse (gccaactctttagggagcaat).

RNA Sequencing Analysis and GSEA. For bulk RNA sequencing, two clonal organoid lines per genotype were cultured in expansion medium for 5 d after which they were washed three times in AdDMEM+++ and cultured for additional 24 h in either expansion medium or a medium lacking EGF. The organoids were then collected in lysis buffer, and the RNA was extracted as previously described. Sequencing libraries were prepared using a modified version of the CELseq2 protocol, and the 75 bp paired-end sequencing of the libraries was performed on the Illumina NextSeq platform. The reads were mapped on the GRCh37 genome assembly, and the differential gene expression analysis was performed using the DESeq2 package. Gene Set Enrichment Analysis (GSEA) was performed using the GSEA v4.1.0 software package (https://www.gsea-msigdb.org/). The enrichment scores (ES) were calculated based on 1,000 gene set permutations. The RNA sequencing dataset has been deposited on Gene Expression Omnibus (GEO) with accession number GSE246896.

MPAS Score Calculation. The MPAS score was calculated as previously described (63). In brief, the gene expression of 10 MAPK target genes was computed as $\mathrm{MPAS} = \left(\sum_i^{z_i}\right) / \left(\sqrt{n}\right)$ where z_i is the z-score of each gene's expression level and i is the number of genes (i.e., i = 10).

Sample Preparation for Proteomics Analyses. Organoid material was lysed in 8 M urea and 50 mM ammonium bicarbonate, supplemented with EDTA-free protease inhibitor (cOmplete Mini, Roche Diagnostics) and phosphatase inhibitor (PhosSTOP, Roche Diagnostics) by vortexing and sonication. Lysates were cleared by centrifugation at 20,000 *g* for 1 h at 15 °C. The protein content of the supernatant was determined using the Bradford protein assay (Bio-Rad). The samples were split into two parts, 25 mg for ubiquitinated proteome analysis and 1 mg for phosphoproteome analysis. Proteins were reduced in 10 mM dithiothreitol at 20 °C for 1 h and then alkylated in 20 mM iodoacetamide at 20 °C for 30 min in the dark. Samples were diluted with 50 mM ammonium bicarbonate to a final concentration of urea <2 M. Lys-C (Wako, Japan) was added for digestion at an enzyme/protein ratio of 1/75 and incubated for 4 h at 37 °C, followed by trypsin (Sigma) at an enzyme/protein ratio of 1/75 and incubated overnight at 37 °C. Digested peptides were purified using Sep-Pak tC18 cartridges (Waters, Ireland) and dried by vacuum centrifugation.

For ubiquitinated proteome analysis, peptides were redissolved in 10 mL of phosphate-buffered saline (PBS) for immunoprecipitation with ubiquitin branch motif (K-ε-GG) antibody bead conjugate (Cell Signaling Technology) at 4 °C and with end-to-end rotation. The beads were washed twice with cold PBS, and the ubiquitinated peptides were eluted using 500 μL of 0.15% trifluoroacetic acid in water. Eluted peptides were desalted using Sep-Pak tC18 cartridges (Waters, Ireland). Phosphorylated peptides were enriched as described before (64) using the AssayMAP Bravo Platform (Agilent Technologies). AssayMAP 5 μL Fe(III)-NTA cartridges (Agilent Technologies) were primed with 250 μL priming buffer (99% ACN/0.1% TFA) and subsequent equilibrate with 250 μL loading buffer (80% ACN and 0.1% TFA). Samples were reconstituted with 210 μL loading buffer, and 200 μL samples were loaded onto the cartridge. After washing with 250 μL loading buffer, phosphorylated peptides were eluted with 50 μL 1% ammonia into the collection plate with 50 μL 10% formic acid. All samples were dried by vacuum centrifugation and stored at −80 °C.

LC–MS/MS Analyses. The analyses were performed as previously described (65). Peptides were reconstituted in 2% formic acid, and triplicate injections were analyzed on an Orbitrap Exploris 480 mass spectrometer (Thermo Scientific), coupled to an UltiMate 3000 UHPLC system (Thermo Scientific). Solvent A was 0.1% formic acid in water, and solvent B was 0.1% formic acid in 80% acetonitrile and 20% water. Peptides were first trapped on an μ-precolumn (C18 PepMap100, 5 μm, 100 Å, 5 mm × 300 μm; Thermo Scientific) in 9% solvent B and then separated on an analytical column (120 EC-C18, 2.7 μm, 50 cm × 75 μm; Agilent Poroshell). The flow rate was kept at 300 nL/min. Peptides from K-ε-GG pulldown were separated on a 155-min gradient, as follows: 10 to 38% in 155 min, 38 to 99% in 3 min, 99% for 4 min, and finally 99 to 9% in 1 min. Phosphopeptides were separated with the gradient as follows: 9 to 36% in 97 min, 36 to 99% in 3 min, 99% for 3 min, and finally 99 to 9% in 1 min. For proteome analysis, peptides from the flowthrough of phospho-enrichment were analyzed in the gradient as follows: 9 to 13% in 1 min, 13 to 44% in 155 min, 44 to 99% in 3 min, 99% for 4 min, and finally 99 to 9% in 1 min.

Eluting peptides were online-injected into the mass spectrometer for data-dependent acquisition. The temperature of the ion transfer tube was set to 275 °C and a RF lens voltage of 40%. MS scans were acquired at a resolution of 60,000 within the m/z range of 375 to 1,600, accumulating to "Standard" preset automated gain control (AGC) target. Multiply charged precursor ions starting from m/z 120 were selected for further fragmentation. Higher-energy collisional dissociation (HCD) was performed with 28% normalized collision energy (NCE), at a resolution of 30,000, with 1.4 m/z isolation window and dynamic exclusion of 24 s for proteome and ubiquitinome and 16 s for phosphoproteome.

Raw Data Processing. MS data were acquired with Thermo Scientific Xcalibur version 4.4.16.14, and raw files were processed using MaxQuant software version 1.6.17.0 with the integrated Andromeda search engine. Data were searched against the human UniProt database including common contaminants (downloaded in April 2021, containing 196,111 entries). For all files, standard parameter settings were used with the enabled the label-free quantification (LFQ) algorithm. Trypsin/P was set as the digestion enzyme (cleaves after lysine and arginine also if a proline follows), and up to two missed cleavages were tolerated. The match-between-run feature was enabled for identification. A false discovery rate (FDR) of 1% was used for peptide and protein identification. Cysteine carbamidomethylation was included as a fixed modification. Protein N-terminal acetylation and methionine oxidation were allowed as variable modifications for all searches, with added GlyGly (K) for ubiquitinated proteome analysis and Phospho (STY) for phosphoproteome analysis.

Data Analysis. Data were analyzed using Perseus software version 1.6.15.0. LFQ intensities of proteins were log2 transformed. Proteins quantified in two out of three replicates in one organoid line were retained for further analysis, after imputation based on the normal distribution. For phosphoproteome analysis, phosphosites with localization probability exceeding 0.75 were retained. To filter for significant changes between experimental conditions two-sided unpaired Student's *t* test was performed. FDR-corrected *P*-values (*q*-values) were calculated from 250 randomizations and considered significant if they were 0.05 or less.

Drug Screening. Drug screenings were performed as previously described (60). In brief, 2 d prior to the drug screening, the organoids were recovered from BME using ice-cold AdDMEM+++ and dissociated into small clumps using TrypLE before being filtered through a 70 μM cell strainer, after which they were replated in fresh BME and cultured in a medium containing 0.5 ng/mL of EGF. Two days later, the organoids were collected with Dispase, counted, and dispensed in a 384-well plate (Corning) at a density of 1,000 organoids per 40 μL of low Egf culture medium supplemented with 8% BME using a Multidrop Combi Reagent Dispenser (Thermo Scientific). The drugs were added thereafter using the Tecan D300e digital dispenser (Tecan). Five days later, ATP levels were measured using the CellTiter-Glo 3-D Reagent (Promega) according to the manufacturer's instructions, and the luminescence was measured with the Spark multimode microplate reader (Tecan). The results were normalized to vehicle (100% viability) while Staurosporine was used as control for maximum cell death. The quality of the drug screen was evaluated with the Z factor scores for each plate following the following formula:

$$\text{Z factor} = 1 - \frac{3 \times \text{SD (negative control)} + 3 \times \text{SD (positive control)}}{\text{average (negative control)} - \text{average (positive control)}}.$$

Only drug screens with a Z factor ≥0.4 were used for the analyses, and the kill curves were plotted with GraphPad software using the option "log (inhibitor) versus normalized response-variable slope."

The following drugs were used for these experiments: Afatinib (#S1011, Selleckchem), Cetuximab (Leftover from clinical use), and Trametinib (#S2673, Selleckchem).

Collection of Clinical Data. The clinical data presented in this study were collected, analyzed, and made available by the Hartwig Medical Foundation and the Center for Personalized Cancer Treatment (CPCT). Further analysis was performed to investigate the effect of FBXW7 mutations on disease progression through anti-EGFR treatment. The data are presented in Dataset S7.

Data, Materials, and Software Availability. The mass spectrometry proteomics data have been deposited to the ProteomeXchange Consortium via the PRIDE partner repository with the dataset identifier PXD049708 (66). All statistical analyses and bar graphs were elaborated with GraphPad Prism V7.03 while heatmaps were made in R. The RNA sequencing dataset has been deposited on Gene Expression Omnibus (GEO) with accession number GSE246896 (67). All other data are included in the manuscript and/or supporting information.

ACKNOWLEDGMENTS. We thank Stieneke van den Brink for the production of R-spondin1-conditioned medium, essential for the organoid expansion medium. This work was supported by an award from the Cancer Research UK Grand Challenge (C6307/A29058) and the Mark Foundation for Cancer Research to the SPECIFICANCER team (H.C., M.H.G., G.-W.H., and M.C.) and by the Netherlands Organ-on-Chip Initiative, an NWO Gravitation project (024.003.001) funded by the Ministry of Education, Culture and Science of the government of the Netherlands. M.B. is a postdoctoral researcher supported by a long-term EMBO fellowship (ALTF 769-2019).

Author affiliations: [a]Organoid group, Oncode Institute, Hubrecht Institute, Royal Netherlands Academy of Arts and Sciences and University Medical Center, 3584 CT Utrecht, the Netherlands; [b]Department of Molecular and Cellular Biology, Miller Institute for Basic Research in Science, University of California, Berkeley, CA 94720; [c]Singapore Immunology Network, Agency for Science, Technology and Research, Singapore 138648, Singapore; [d]Department of Pharmacy, National University of Singapore, Singapore 117543, Singapore; [e]Department of Biomolecular Mass Spectrometry and Proteomics, Biomolecular Mass Spectrometry and Proteomics, Bijvoet Center for Biomolecular Research and Utrecht Institute for Pharmaceutical Sciences, Utrecht University, 3584 CH Utrecht, the Netherlands; and [f]Department of Medical Oncology, University Medical Center Utrecht, 3584 CX Utrecht, the Netherlands

1. T. Ravid, M. Hochstrasser, Diversity of degradation signals in the ubiquitin–proteasome system. *Nat. Rev. Mol. Cell Biol.* **9**, 679–689 (2008).
2. A. Ciechanover, The ubiquitin-proteasome proteolytic pathway. *Cell* **79**, 13–21 (1994).
3. A. Mani, E. P. Gelmann, The ubiquitin-proteasome pathway and its role in cancer. *J. Clin. Oncol.* **23**, 4776–4789 (2005).
4. G. Nalepa, M. Rolfe, J. W. Harper, Drug discovery in the ubiquitin–proteasome system. *Nat. Rev. Drug. Discov.* **5**, 596–613 (2006).
5. Z. Ge *et al.*, Integrated genomic analysis of the ubiquitin pathway across cancer types. *Cell Rep.* **23**, 213–226.e3 (2018).
6. D. Hoeller, I. Dikic, Targeting the ubiquitin system in cancer therapy. *Nature* **458**, 438–444 (2009).
7. K. I. Nakayama, K. Nakayama, Ubiquitin ligases: Cell-cycle control and cancer. *Nat. Rev. Cancer* **6**, 369–381 (2006).
8. F. Martínez-Jiménez, F. Muiños, E. López-Arribillaga, N. Lopez-Bigas, A. Gonzalez-Perez, Systematic analysis of alterations in the ubiquitin proteolysis system reveals its contribution to driver mutations in cancer. *Nat. Cancer. NLM (Medline)* **1**, 122–135 (2020).
9. B. Mészáros, M. Kumar, T. J. Gibson, B. Uyar, Z. Dosztányi, Degrons in cancer. *Sci. Signal* **10**, eaak9982 (2017).
10. M. Welcker, B. E. Clurman, FBW7 ubiquitin ligase: A tumour suppressor at the crossroads of cell division, growth and differentiation. *Nat. Rev. Cancer* **8**, 83–93 (2008).
11. B. Hao, S. Oehlmann, M. E. Sowa, J. W. Harper, N. P. Pavletich, Structure of a Fbw7-Skp1-Cyclin E complex: Multisite-phosphorylated substrate recognition by SCF ubiquitin ligases. *Mol. Cell* **26**, 131–143 (2007).
12. M. Welcker *et al.*, Fbw7 dimerization determines the specificity and robustness of substrate degradation. *Genes Dev.* **27**, 2531–2536 (2013).
13. S. Orlicky, X. Tang, A. Willems, M. Tyers, F. Sicheri, Structural basis for phosphodependent substrate selection and orientation by the SCFCdc4 ubiquitin ligase. *Cell* **112**, 243–256 (2003).
14. D. M. Koepp *et al.*, Phosphorylation-dependent ubiquitination of cyclin E by the SCF ^{Fbw7} ubiquitin ligase. *Science* **1979**, 173–177 (2001).
15. M. Welcker *et al.*, Multisite phosphorylation by Cdk2 and GSK3 controls cyclin E degradation. *Mol. Cell* **12**, 381–392 (2003).
16. C.-M. Xie *et al.*, The FBXW7-SHOC2-raptor axis controls the cross-talks between the RAS-ERK and mTORC1 signaling pathways. *Cell Rep.* **26**, 3037–3050.e4 (2019).
17. A. Arabi *et al.*, Proteomic screen reveals Fbw7 as a modulator of the NF-κB pathway. *Nat. Commun.* **3**, 976 (2012).
18. H. Inuzuka *et al.*, SCFFBW7 regulates cellular apoptosis by targeting MCL1 for ubiquitylation and destruction. *Nature* **471**, 104–109 (2011).
19. H. Rajagopalan *et al.*, Inactivation of hCDC4 can cause chromosomal instability. *Nature* **428**, 77–81 (2004).
20. H. Strohmaier *et al.*, Human F-box protein hCdc4 targets cyclin E for proteolysis and is mutated in a breast cancer cell line. *Nature* **413**, 316–322 (2001).
21. R. Sancho, R. Gruber, G. Gu, A. Behrens, Loss of Fbw7 reprograms adult pancreatic ductal cells into α, δ, and β cells. *Cell Stem Cell* **15**, 139–153 (2014).
22. N. Singh, A. Zeke, A. Reményi, Systematic discovery of FBXW7-binding phosphodegrons highlights mitogen-activated protein kinases as important regulators of intracellular protein levels. *Int. J. Mol. Sci. MDPI* **23**, 3320 (2022).
23. B. Pérez-Benavente *et al.*, GSK3-SCF FBXW7 targets JunB for degradation in G2 to preserve chromatid cohesion before anaphase. *Oncogene* **32**, 2189–2199 (2013).
24. C.-J. Lee *et al.*, FBXW7-mediated stability regulation of signal transducer and activator of transcription 2 in melanoma formation. *Proc. Natl. Acad. Sci. U.S.A.* **117**, 584–594 (2020).
25. X. Zhao *et al.*, Circadian amplitude regulation via FBXW7-targeted REV-ERBα degradation. *Cell* **165**, 1644–1657 (2016).
26. S. Singh *et al.*, Loss of ELF5–FBXW7 stabilizes IFNGR1 to promote the growth and metastasis of triple-negative breast cancer through interferon-γ signalling. *Nat. Cell Biol. Nat. Res.* **22**, 591–602 (2020).
27. D. Cui *et al.*, FBXW7 confers radiation survival by targeting p53 for degradation. *Cell Rep.* **30**, 497–509.e4 (2020).
28. N. Kourtis *et al.*, FBXW7 modulates cellular stress response and metastatic potential through HSF1 post-translational modification. *Nat. Cell Biol.* **17**, 322–332 (2015).
29. N. Li *et al.*, An FBXW7-ZEB2 axis links EMT and tumour microenvironment to promote colorectal cancer stem cells and chemoresistance. *Oncogenesis* **8**, 13 (2019).
30. S. O'Brien *et al.*, SCF ^{FBXW7} regulates G2-M progression through control of CCNL1 ubiquitination. *EMBO Rep.* **23**, e55044 (2022).
31. B. King *et al.*, The ubiquitin ligase FBXW7 modulates leukemia-Initiating cell activity by regulating MYC stability. *Cell* **153**, 1552–1566 (2013).
32. D. M. Muzny *et al.*, Comprehensive molecular characterization of human colon and rectal cancer. *Nature* **487**, 330–337 (2012).
33. R. L. Siegel, K. D. Miller, H. E. Fuchs, A. Jemal, Cancer statistics, 2022. *CA Cancer J. Clin.* **72**, 7–33 (2022).
34. P. A. J. Mendelaar *et al.*, Whole genome sequencing of metastatic colorectal cancer reveals prior treatment effects and specific metastasis features. *Nat. Commun.* **12**, 574 (2021).
35. L. Lupini *et al.*, Prediction of response to anti-EGFR antibody-based therapies by multigene sequencing in colorectal cancer patients. *BMC Cancer* **15**, 808 (2015).
36. A. M. Rachiglio *et al.*, Genomic profiling of KRAS/NRAS/BRAF/PIK3CA wild-type metastatic colorectal cancer patients reveals novel mutations in genes potentially associated with resistance to anti-EGFR agents. *Cancers (Basel)* **11**, 859 (2019).
37. T. Sato *et al.*, Long-term expansion of epithelial organoids from human colon, adenoma, adenocarcinoma, and Barrett's epithelium. *Gastroenterology* **141**, 1762–1772 (2011).
38. J. Drost *et al.*, Sequential cancer mutations in cultured human intestinal stem cells. *Nature* **521**, 43–47 (2015).
39. B. Artegiani *et al.*, Probing the tumor suppressor function of BAP1 in CRISPR-engineered human liver organoids. *Cell Stem Cell* **24**, 927–943.e6 (2019).
40. M. H. Geurts *et al.*, CRISPR-based adenine editors correct nonsense mutations in a cystic fibrosis organoid biobank. *Cell Stem Cell* **26**, 503–510.e7 (2020).
41. N. M. Gaudelli *et al.*, Programmable base editing of A•T to G•C in genomic DNA without DNA cleavage. *Nature* **551**, 464–471 (2017).
42. L. W. Koblan *et al.*, Improving cytidine and adenine base editors by expression optimization and ancestral reconstruction. *Nat. Biotechnol.* **36**, 843–846 (2018).
43. A. C. Komor, Y. B. Kim, M. S. Packer, J. A. Zuris, D. R. Liu, Programmable editing of a target base in genomic DNA without double-stranded DNA cleavage. *Nature* **533**, 420–424 (2016).
44. M. P. Zafra *et al.*, Optimized base editors enable efficient editing in cells, organoids and mice. *Nat. Biotechnol.* **36**, 888–893 (2018).
45. A. Andersson-Rolf *et al.*, One-step generation of conditional and reversible gene knockouts. *Nat. Methods* **14**, 287–289 (2017).
46. M. H. Geurts *et al.*, Evaluating CRISPR-based prime editing for cancer modeling and CFTR repair in organoids. *Life Sci. Alliance* **4**, e202000940 (2021).
47. M. Fujii, M. Matano, K. Nanki, T. Sato, Efficient genetic engineering of human intestinal organoids using electroporation. *Nat. Protoc.* **10**, 1474–1485 (2015).
48. K. F. Marquart *et al.*, Predicting base editing outcomes with an attention-based deep learning algorithm trained on high-throughput target library screens. *Nat. Commun.* **12**, 5114 (2021).
49. E. R. Fearon, B. Vogelstein, A genetic model for colorectal tumorigenesis. *Cell* **61**, 759–67 (1990).
50. M. Matano *et al.*, Modeling colorectal cancer using CRISPR-Cas9-mediated engineering of human intestinal organoids. *Nat. Med.* **21**, 256–262 (2015).
51. T. Seino *et al.*, Human pancreatic tumor organoids reveal loss of stem cell niche factor dependence during disease progression. *Cell Stem Cell* **22**, 454–467.e6 (2018).
52. D. M. Freed *et al.*, EGFR ligands differentially stabilize receptor dimers to specify signaling kinetics. *Cell* **171**, 683–695.e18 (2017).
53. M. Fujii *et al.*, Human intestinal organoids maintain self-renewal capacity and cellular diversity in niche-inspired culture condition. *Cell Stem Cell* **23**, 787–793.e6 (2018).
54. G. J. Heisermann *et al.*, Mutational removal of the Thr669 and Ser671 phosphorylation sites alters substrate specificity and ligand-induced internalization of the epidermal growth factor receptor. *J. Biol. Chem.* **265**, 12820–12827 (1990).
55. T. Lan *et al.*, Type II cGMP-dependent protein kinase phosphorylates EGFR at threonine 669 and thereby inhibits its activation. *Biochem. Biophys. Res. Commun.* **518**, 14–18 (2019).
56. J. Tong, S. Tan, F. Zou, J. Yu, L. Zhang, FBW7 mutations mediate resistance of colorectal cancer to targeted therapies by blocking Mcl-1 degradation. *Oncogene* **36**, 787–796 (2017).
57. M. Ye *et al.*, Targeting FBW7 as a strategy to overcome resistance to targeted therapy in non-small cell lung cancer. *Cancer Res.* **77**, 3527–3539 (2017).
58. E. Driehuis *et al.*, Oral mucosal organoids as a potential platform for personalized cancer therapy. *Cancer Discov.* **9**, 852–871 (2019).
59. J. F. Seligmann *et al.*, Combined epiregulin and amphiregulin expression levels as a predictive biomarker for panitumumab therapy benefit or lack of benefit in patients with *RAS* wild-type advanced colorectal cancer. *JAMA Oncol.* **2**, 633 (2016).
60. M. van de Wetering *et al.*, Prospective derivation of a living organoid biobank of colorectal cancer patients. *Cell* **161**, 933–945 (2015).

61. F. Weeber *et al.*, Preserved genetic diversity in organoids cultured from biopsies of human colorectal cancer metastases. *Proc. Natl. Acad. Sci. U.S.A.* **112**, 13308–13311 (2015).
62. Amgen Inc., VECTIBIX® (panitumumab) prescribing information (Amgen Inc., Thousand Oaks, CA, 2017).
63. M. C. Wagle *et al.*, A transcriptional MAPK pathway activity score (MPAS) is a clinically relevant biomarker in multiple cancer types. *NPJ Precis Oncol.* **2**, 7 (2018).
64. H. Post *et al.*, Robust, sensitive, and automated phosphopeptide enrichment optimized for low sample amounts applied to primary hippocampal neurons. *J. Proteome Res.* **16**, 728–737 (2017).
65. J. Beumer *et al.*, BMP gradient along the intestinal villus axis controls zonated enterocyte and goblet cell states. *Cell Rep.* **38**, 110438 (2022).
66. M. Boretto *et al.*, Analysis of FBXW7 mutants in colon organoids. PRIDE Proteomics Identifications Database. https://www.ebi.ac.uk/pride/archive/projects/PXD049708. Deposited 4 October 2021.
67. M. Boretto *et al.*, EGFR is a target of the tumor suppressor E3-ligase FBXW7. GEO. https://www.ncbi.nlm.nih.gov/geo/query/acc.cgi?acc=GSE246896. Deposited 2 November 2023.